Artifact Suppressed Nonlinear Diffusion Filtering for Low-Dose CT Image Processing

YI LIU[1], **YANG CHEN**[2], **PING CHEN**[3], **ZHIWEI QIAO**[4], **AND ZHIGUO GUI**[1]

[1]Shanxi Provincial Key Laboratory for Biomedical Imaging and Big Data, North University of China, Taiyuan 030051, China
[2]LIST, Key Laboratory of Computer Network and Information Integration, Ministry of Education, Southeast University, Nanjing 210096, China
[3]School of Information and Communication Engineering, North University of China, Taiyuan 030051, China
[4]School of Computer and Information Technology, Shanxi University, Taiyuan 030006, China

Corresponding author: Zhiguo Gui (gzgtg@163.com)

ABSTRACT Computed tomography (CT) images with a low-dose protocol generally have severe mottle noise and streak artifacts. In this paper, we propose a novel diffusion method named ''artifact suppressed nonlinear diffusion filtering (ASNDF),'' to process low-dose CT (LDCT) images. Different from other diffusion filtering methods, the proposed ASNDF not only includes image gradient as the main cue to construct a diffusion coefficient function, but also incorporates the local variances of image to be diffused and residual image between two adjacent diffusions. In detail, the classical PM diffusion is first performed to get the initial residual image, and then from the second iteration, the LDCT image is processed according to the ASNDF processing. Simulated data, clinical data and rat data are conducted to evaluate the proposed method, and the comparison experiments with other competing methods show that the proposed ASNDF method makes an improvement in artifact suppression and structure preservation, and offers a sound alternative to process LDCT images from most current CT systems.

INDEX TERMS Low-dose computed tomography, nonlinear diffusion, local variance, residual local variance.

I. INTRODUCTION

Low-dose computed tomography (LDCT) was first proposed by Naidich in 1990 for the reason that the radiation doses delivered to patients during X-ray CT procedures may lead to potential determinist and stochastic risks [1]. Nowadays, the issue of X-ray CT radiation dose is raising more and more concerns, especially for children and patients who need to undergo several CT examinations in a short period [2]–[6]. Although radiation dose reduction is beneficial for human health, it leads to the filtered back projection (FBP) reconstructed images degraded with serious mottle noise and streak artifacts [7], [8]. Noise and streak artifacts suppression for LDCT images is therefore required and there are generally three strategies so far to improve the quality of LDCT images: projection domain denoising, iterative reconstruction algorithms and post-processing methods.

The first one refers to techniques that suppress the excessive quantum noise in projection data before performing FBP reconstruction. Many denoising approaches have been proposed to deal with the noisy projection data, such as multi-dimensional adaptive filtering [9], nonlinear filtering [10], penalized weighted least-squares (PWLS) approaches [11], [12], bilateral filtering [13], fuzzy filtering [14], [15], and iterative restoration [16]. Other techniques, such as the bilateral-like filter [17], multi-scale decomposition based method [18], also have potentials to process noisy projection data. Denoising in projection domain takes noise property of projection data into account, but it needs access to projected raw data from CT vendors, which makes researchers in this direction limited to some extent. Iterative reconstruction approaches consists in finding an optimal solution by maximizing or minimizing an objective function regularized by prior terms. The prior design is the key and many edge-preserving priors have been proposed in the past decades, for example, Huber prior [19], [20],

total-variation (TV) based priors [21], [22], nonlocal priors [23], [24], anisotropic priors [25], Markov random field (MRF)-based prior [26], and bilateral prior [27]. In iterative reconstruction noise and artifacts can be modeled, and an appropriate prior or an adjusted forward model can be designed to reduce artifacts. However, they also need the access to projected raw data from CT vendors and suffer from high computation cost. Those limitation in both projection restoration and iterative reconstruction lead us to consider post-processing methods, which can be retrospectively applied on different systems.

Post-processing methods are relatively simple to implement and can be applied directly on reconstructed LDCT images with no requirement of raw projection data. The challenge is to remove mottle noise and streak artifacts without damaging structures and details. In the past decade, various techniques have been proposed to improve the quality of LDCT images, such as nonlocal means (NLM) denoising [28]–[30], dictionary learning (DL) based denoising [31], [32], and block-matching 3D (BM3D) denoising [33], [34]. Most of these methods take structure similarity into account, therefore they can improve CT images significantly. Recently, deep learning based on convolution neural network (CNN) is popular in image denoising [35]–[37], and can be used for LDCT images. But the results of CNNs depend on training data, and it takes a long time to train a CNN model.

The nonlinear diffusion filtering (NDF) is a useful technique for filtering noise from images. It is derived from the well-known Perona-Malik nonlinear diffusion model [38], which uses an edge seeking function to encourage diffusion within regions and prohibit it across strong edges. Hence edges can be preserved while removing noise from the image. However, PM model often suffers from staircase effect and removes fine details as noise. In order to overcome these problems, improved versions have been proposed [39]–[41] and are used to process all kinds of images, including LDCT images. Mendrik *et al.* [42] proposed a hybrid diffusion model that combines edge-enhancing diffusion and coherence-enhancing diffusion in a continuous manner and applied it to simulated low-dose CT scan. Saito *et al.* [43] improved the nonlinear diffusion filtering by determining in a theoretical manner the value of the parameter required for calculating diffusivities, and applied it to LDCT perfusion images. Yang *et al.* [44] presented a multi-resolution nonlinear anisotropic diffusion method using Laplace pyramid decomposition to remove noise/artifacts in LDCT images. Similarly, Liu *et al.* [18] modified the classical edge seeking function in PM and performed the diffusion process in Laplace pyramid domain to improve abdominal low-dose cone beam CT. Wang *et al.* [45] proposed a new fractional-order model named FPMTV by integrating fractional PM model and fractional TV model to suppress noise for LDCT.

In summary, although the NDF methods mentioned above can improve LDCT images to varying degrees, they may fail to keep fine details and small structures well when suppressing artifacts greatly, because most of them still employ image gradient magnitude as the main cue of edge indicator, which is not proper for LDCT images. With regard to LDCT images, orientation in artifacts is prominent, streak artifacts therefore may lead to similar gradient magnitudes as edges or textures, and will be retained in the diffusion process.

To remove streak artifacts in LDC images more effectively, in this paper, we propose artifact suppressed nonlinear diffusion filtering (ASNDF) based on PM model to improve LDCT images. In the proposed ASNDF, a new diffusion coefficient function is proposed, in which both the image local variance and residual local variance (between two adjacent diffusions) are introduced to be the cue of edge/detail indicator. The image local variance can effectively indicate strong edges and especially distinguish details and noisy background, whereas the residual local variance is more effective to indicate location where weak textures and fine details are. Specifically, both of them are not sensitive to smooth regions and streak artifacts in LDCT images, thus the new diffusion coefficient inhibits diffusion in edges, textures and fine details, and encourage diffusion in streak artifacts and smooth regions. Experiments on different simulated data, clinical data and in-vitro rat data were conducted to show the good performance of the proposed algorithm.

This paper is organized as follows: In Section II, we mainly describe the classical PM diffusion and the proposed algorithm. Experimental settings and results are given and discussed in Section III. Conclusions and plans for future work are in Section IV.

II. MATERIALS AND METHODS
To overcome the drawback that only image gradient magnitude is used to be the main cue of edge indicator, and effectively suppress artifacts in LDCT images, we propose the ASNDF method based on PM model. The novelty of the proposed method is that, in addition to gradient image, we also employ image local variance and residual local variance as edge/detail indicators, and design suitable combinations of these indicators to construct a new diffusion coefficient function.

The image local variance itself is a high pass filter and has been used as edge/detail indicator in [46] and [47]. Residual image (also named method noise) is defined as the difference between the noisy image and its filtered version, thus it contains high frequency information of details lost in filtering. Many studies have utilized the high frequency information in residual image to remove noise and meanwhile to preserve image details [48]–[50]. In this paper, we combine image local variance, residual local variance, and image gradient to construct the diffusion coefficient function, which is more effective to control diffusion degree in edge/detail regions that are contaminated with noise/artifacts. Since the proposed method refers to the PM model, we first illustrate it in the following section.

A. PM NONLINEAR DIFFUSION

The classical anisotropic diffusion with PM model employs the image gradient to derive different diffusion intensities in different directions. The PM process is described by

$$I_t = div\left(c\left(\nabla I\right)\nabla I\right), \quad I_{t=0} = I_0, \tag{1}$$

where div and ∇ is the divergence operator and gradient operator, respectively. c stands for the diffusion coefficient and determines the diffusion degree. I_t is the denoised image with respect to the initial image I_0. The suggested two diffusion coefficient functions are

$$c_1\left(|\nabla I|\right) = \frac{1}{1 + \left(|\nabla I|/k\right)^2}, \tag{2}$$

$$c_2\left(|\nabla I|\right) = \exp\left(-\left(|\nabla I|/k\right)^2\right), \tag{3}$$

where k is a threshold parameter. Given a k, we can easily understand from (2) and (3) that a large gradient magnitude (often happen in edges) contributes to a small diffusion coefficient, thus the smoothing effect is negligible. Conversely, a small gradient magnitude (happen in the smooth regions) has a large diffusion coefficient and consequently the smoothing effect is significant.

B. ARTIFACT SUPPRESSED NONLINEAR DIFFUSION FILTERING

Although PM diffusion is useful in permitting edges, some textures and fine details are removed during the diffusion process, furthermore, staircase effective may be introduced in the final diffused image. This is because that gradient-based edge indicator is not a proper measure to detect weak textures and fine details whose gradient magnitudes may be similar to noise. In addition, for LDCT images, streak artifacts could be easily retained as the strong orientation in artifacts. In this part, we present a new anisotropic diffusion model that incorporates image gradient, image local variance, and residual local variance for adaptive noise/artifacts suppression and edges/details preserving.
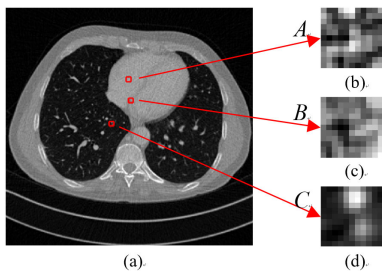

FIGURE 1. LDCT slice of the abdomen. (a) Original image; (b) Sub-image from a smooth region; (c) Sub-image from a texture-like detail and (d) sub-image from small structure.

1) IMAGE LOCAL VARIANCE

In addition to the image gradient magnitude, image local variance is also can be seen as an edge indicator. Fig. 1(a) presents a LDCT slice of abdomen, in which we can see strong edges,

many fine details and also artifacts/noise dispersed in the entire image. Fig. 1(b)-(d) are three enlarged sub-images from Fig. 1(a), marked as A, B, and C, indicating the homogeneous region, fine detail and small structure, respectively. The mean gradient magnitudes in (b)-(d) are 250.23, 243.53 and 161.24, respectively, namely Region A and Region B have similar gradient magnitudes, and both are larger than Region C. Therefore, the conventional anisotropic diffusion model may have similar degree of diffusion in Region A and Region B since the gradient values in Fig. 1(b) and (c) are similar, and more severe diffusion in Region C since the gradient value in Fig. 1(d) is lower. As a result, the fine detail and small structure will be blurred and the small structure even may vanish in the final diffused image.

The variances of images (b)-(d) in Fig. 1 are 3676, 7001, and 6328, respectively. Obviously, they are distinctly different compared with the gradient magnitudes and seems a more reasonable indicator to control diffusion. There is no doubt that the neighborhood in strong edges, e.g., inter-region edges, generally has both high gradient magnitude and large variance. The observation from this demonstrated image reveals that the fine detail and noisy homogeneous region have smaller gradient strength, but the variances in fine detail and small structure are larger than that in the noisy homogeneous region. To be specific, although the small structure has lower gradient magnitude, it has a relative higher local variance. Fig. 2(b) illustrates the local variance image at 20th iteration when using PM model to process the LDCT image in Fig. 1(a). We can observe that edges and most detail regions are bright, therefore, local variance could be considered as a local pixel feature in the diffusion coefficient.
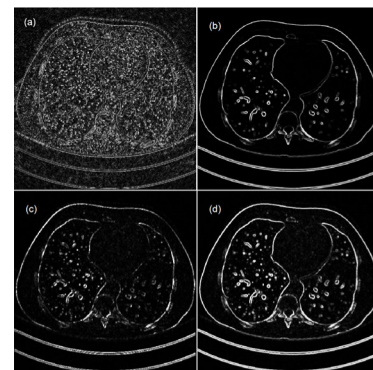
FIGURE 2. Images at 20th iteration in the PM diffusion process. (a) Residual image, (b) local variance, (c) residual local variance and (d) the plus of image (b) and image (c).

For a given pixel of coordinates (i, j) at iteration t, the local variance is defined as

$$\sigma_{I_t}^2(i, j) = \frac{1}{9}\sum_{k=-1}^{1}\sum_{l=-1}^{1}\left[I_t\left(i+k, j+l\right) - \bar{I}_t\left(i, j\right)\right]^2, \tag{4}$$

where $\bar{I}\left(i, j\right)$ is the mean intensity in the 3×3 neighborhood of pixel $I\left(i, j\right)$. Since the range of variance is dramatically larger than that of gradient magnitude, we down-scaled the

variance so that it is compatible to the gradient magnitude. The variance is scaled as suggested in [49],

$$\sigma_{I_t,scaled}^2(i,j) = \frac{\sigma_{I_t}^2(i,j) - \text{Min}\sigma_{I_t}^2}{\text{Max}\sigma_{I_t}^2 - \text{Min}\sigma_{I_t}^2} \cdot (\max(|\nabla I_t|) - 1) + 1,$$

(5)

where $\text{Min}\sigma_{I_t}^2$ and $\text{Max}\sigma_{I_t}^2$ are the minimum and maximum variances of the diffused image at iteration t, respectively.

The image local variance has proposed to improve the PM method by Chao in [40], and the improved PM (IPM) method has been proved effective for retaining fine details. The diffusion coefficient function in [40] is defined as

$$c\left(|\nabla I|, \sigma_{I_t,scaled}^2\right) = 1 \bigg/ \left[1 + \left(\left(|\nabla I| \cdot \sigma_{I_t,scaled}^2\right)\bigg/k\right)^2\right].$$

(6)

Since this diffusion coefficient function takes both $|\nabla I|$ and $\sigma_{I_t,scaled}^2$ in to account, it can effectively distinguish details and noisy homogeneous regions. However, the IPM method cannot be well applied to the images containing high-level noise and sparking impulse noise. In LDCT images, artifacts/noise are serious, which can be seen as high-level noise. Therefore, although the image local variance is useful to distinguish details and noisy homogeneous regions, the IPM method may fail to perform well on a very noisy LDCT image. What we need to do is to find a more suitable way to use the image local variance.

2) RESIDUAL LOCAL VARIANCE
The residual image in our study is defined as the different image between two adjacent diffusions, i.e.,

$$R(t) = I(t-1) - I(t).$$

(7)

The residual image includes both signal components, e.g. fine details, and artifacts/noise components. Fig. 2(a) shows the residual image at 20th iteration when using PM model to process the LDCT image in Fig. 1(a). We observed that it contains rich information of details and noise/artifacts as well. We also calculate the local variances of the Region *A*, *B*, and *C* in the residual image. They are 1.01, 1.24, and 2.86, respectively. Obviously, the local variances in fine detail and small structure are higher than that in smooth region, especially the small structure has the highest variance. Therefore, it seems that the residual local variance could be considered as a reasonable feature to indicate small structures in the diffusion process. Of course, $R(t)$ contains less and less information along with iterations, but this does not prevent us to utilize it before the diffusion is stopped according to a criterion. We also calculate all pixels' local variance for the residual image and show it in Fig. 2(c). The definition of residual local variance is similar to (4).

$$\sigma_{R_t}^2(i,j) = \frac{1}{9}\sum_{k=-1}^{1}\sum_{l=-1}^{1}\left[R_t(i+k,j+l) - \bar{R}_t(i,j)\right]^2,$$

(8)

where $\bar{R}_t(i,j)$ is the mean intensity in the 3×3 neighborhood of a given pixel of coordinates (i,j) at iteration t. Similar to local variance, we also down-scale the residual local variance.

$$\sigma_{R_t,scaled}^2(i,j) = \frac{\sigma_{R_t}^2(i,j) - \text{Min}\sigma_{R_t}^2}{\text{Max}\sigma_{R_t}^2 - \text{Min}\sigma_{R_t}^2} \cdot (\max(|\nabla I_t|) - 1) + 1,$$

(9)

where $\text{Min}\sigma_{R_t}^2$ and $\text{Max}\sigma_{R_t}^2$ are the minimum and maximum variances of the residual image at iteration t, respectively.

As we observe in Fig. 2(c), edge and detail regions, especially the later, are brighter, denoting that residual local variance is sensitive to fine details. So, the residual local variance could be another detail detection indicator besides local variance. One advantage of using this residual local variance in diffusion is that if some edges or details are wrongly removed during the diffusion process, it appears in residual local variance and consequently can be preserved.

Since both the local variances of diffused image I and residual image R can indicate edges and details, we confidently integrate them to be as a new edge and detail detector. In Fig. 2(d), we show a combination (using plus operator) of image local variance and residual local variance at the 20th iteration. We observe that more small structures can be seen in Fig. 2(d), compared to Fig. 2(b), that's, fine details that maybe cannot detected using image local variance, but can be detected by using residual local variance.

3) THE PROPOSED METHOD
According to analysis mentioned above, we can find that the image local variance can effectively indicate strong edges and especially distinguish details and noisy homogeneous regions, whereas the residual local variance is more effective to indicate where much weaker details are. Specifically, we can observe that components of streak artifacts in Fig. 2(b)-(d) are not dominant, this means that streak artifacts could be effectively suppressed if we employ image local variance and residual local variance to control the diffusion process. Therefore, we propose an ASNDF method wherein both image local variance and residual local variance are incorporated to design the new diffusion coefficient function as

$$c_{new}\left(|\nabla I|, \sigma_{I_t,scaled}^2, \sigma_{R_t,scaled}^2\right)$$
$$= \frac{1}{3} \times \left[\begin{array}{l} 1 \bigg/ \left[1 + \left(\left(|\nabla I| + \sigma_{I_t,scaled}^2\right)\bigg/k\right)^2\right] \\ +1 \bigg/ \left[1 + \left(\left(|\nabla I| + \sigma_{R_t,scaled}^2\right)\bigg/k\right)^2\right] \\ +1 \bigg/ \left[1 + \left(\left(\sigma_{I_t,scaled}^2 + \sigma_{R_t,scaled}^2\right)\bigg/k\right)^2\right] \end{array}\right].$$

(10)

The new c is the combination of three diffusion coefficient functions and calculates the average. Each term is similar to the diffusion coefficient function of PM but makes a difference.

The first term in (10) is a decreasing function of the sum of image gradient magnitude and scaled image local variance. In homogenous regions, both $|\nabla I|$ and $\sigma^2_{I_t,scaled}$ are small, thus the first term gets its largest value which leads to strongly artifacts/noise removal. In strong edges wherein $|\nabla I|$ and $\sigma^2_{I_t,scaled}$ are large, the first diffusion coefficient has its smallest amount and consequently this region is well preserved. In small structures or details wherein $|\nabla I|$ is small but $\sigma^2_{I_t,scaled}$ is relatively large (as we see in Fig.1), the first coefficient is relatively large and so these regions are preserved. The first term focuses on distinguishing details and artifact-existing homogenous regions which may have similar gradient magnitudes but have a big difference in image local variance. In fact, the image local variance essentially is a high pass filter and similar in appearance to gradient magnitude, but it can effectively distinguish details and noisy background.
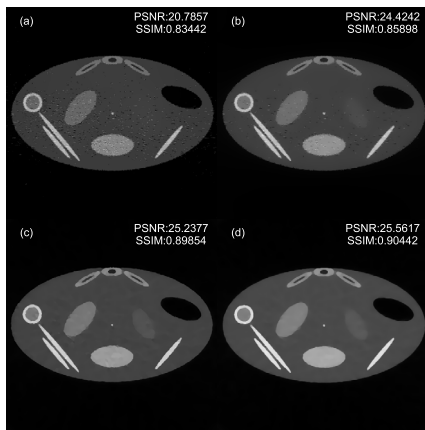
FIGURE 3. The processed LDCT images by using different diffusion coefficient functions. (a) Equation (6), (b) the first term in (10), (c) the second term in (10), and (d) the third term in (10).

Specifically, since $\sigma^2_{I_t,scaled}$ was also used in IPM, we compared our combination way of the two edge indicators ($|\nabla I|$ and $\sigma^2_{I_t,scaled}$) and that in IPM method. We performed the diffusion function of IPM and also the first term in (10) on the LDCT image Recon400 (more details could be found in the "Phantom Data Study"), which has serious noise and artifacts. The IPM processed result is shown in Fig. 3(a), and the PSNR and SSIM results of the processed image is tagged in the right-upper corner (the definition of PSNR and SSIM could be found in (16) and (18)). We can see that it cannot effectively suppress noise and artifacts. We also use the first term $1\left/\left[1+\left(\left(|\nabla I|+\sigma^2_{I_t,scaled}\right)\middle/k\right)^2\right]\right.$ to control the diffusion process, and the result is shown in Fig. 3(b) with the PSNR and SSIM results tagged in the right-upper corner. All parameters in both process are the same. Obviously, Fig. 3(b) has less noise than the IPM processed image. It proves that the way we exploit the local variance is effective and more suitable than the IPM method for LDCT images.

The second term in (10) is a decreasing function of the sum of image gradient magnitude and scaled residual

local variance. In homogenous regions, both $|\nabla I|$ and $\sigma^2_{R_t,scaled}$ are small, thus the second term gets its largest value, leading to strongly artifacts/noise removal. In strong edges, both $|\nabla I|$ and $\sigma^2_{R_t,scaled}$ are large and most edges could be preserved, therefore less is left in the residual image. So the second term becomes from large to relatively small and edges could be preserved in this process. In details, even if in fine details and small structures, $|\nabla I|$ is relatively small but $\sigma^2_{R_t,scaled}$ is large. This makes the second diffusion coefficient relatively large and so details and small structures can be preserved. Specifically, when the residual image becomes to none along with iterations, the second term degrades into the diffusion coefficient function PM.

To prove the effectiveness of the residual local variance for low-dose images, we also use the second term $1\left/\left[1+\left(\left(|\nabla I|+\sigma^2_{R_t,scaled}\right)\middle/k\right)^2\right]\right.$ to control the diffusion process for image Recon400, and the result is shown in Fig. 3(c). We can see that noise and artifacts are effectively removed, showing that the residual local variance is effective for LDCT images.

The third term in (10) is a decreasing function of the sum of scaled image local variance and scaled residual local variance. From Fig. 2(d), we can observe that the sum of $\sigma^2_{I_t,scaled}$ and $\sigma^2_{R_t,scaled}$ are large in edges, details, and structures, whereas in homogeneous regions they are both small. Thus, the third coefficient is effective in preserving edges and details. Since components of artifacts are not obviously reflected both in image local variance and residual local variance, as shown in Fig. 2, artifacts will not prevent the diffusion strength and then can be suppressed.

TABLE 1. PSNR and SSIM results the original and processed images in Fig. 3.

	Fig. 3(a)	Fig. 3(b)	Fig. 3(c)	Fig. 3(d)	Recon400
PSNR	20.7857	24.4242	25.2377	25.5617	23.0854
SSIM	0.83442	0.85898	0.89854	0.90442	0.21573

To further improve the effectiveness of local variance and residual local variance for low-dose images, we also use the third term $1\left/\left[1+\left(\left(\sigma^2_{I_t,scaled}+\sigma^2_{R_t,scaled}\right)\middle/k\right)^2\right]\right.$ as the diffusion coefficient function to control the diffusion process for image Recon400, and the result is shown in Fig. 3(d) with the PSNR and SSIM results tagged in the right-upper corner. We can see that noise and artifacts are significantly removed, showing that the combination of local variance and residual local variance is effective for LDCT images. To show the effectiveness of local variance and residual local variance clearly, we also calculate the PSNR and SSIM results of the LDCT image Recon400. Table 1 lists the PSNR and SSIM results of Recon 400 and the processed images in Fig. 3. We can see that the PSNR and SSIM values of Fig. 3(b)-(d) are higher than those in the original Rcon400, indicating that each term in (10) can improve the LDCT image Rcon400.

In addition, since components of streak artifacts are not dominant in image local variance and residual local variance,

(see Fig. 2(b)-(d)), we will get high diffusion coefficients according to (10), thus there will be a greater diffusion degree and artifacts can be removed. This also proves that the introduction of image local variance and residual local variance is effective to suppress artifacts.

In our study, the threshold k in (10) is automatically set and updated according to the histogram of the gradient magnitude of the diffused image, the value at 90% of the histogram is chosen through trial and error. Additionally, we improve the diffusion coefficient function in (10) by using a Gaussian filter according to [51] since a Gaussian filter for c is beneficial to remove speckle noise. Thus, the diffusion coefficient is redefined in (11) as

$$c_{APNDF}\left(|\nabla I|, \sigma_{I_t,scaled}^2, \sigma_{R_t,scaled}^2\right)$$
$$= c_{new}\left(|\nabla I|, \sigma_{I_t,scaled}^2, \sigma_{R_t,scaled}^2\right) * G_\sigma, \quad (11)$$

where G_σ is a Gaussian kernel of 3×3 size and standard deviation σ. When σ is small, the filtering of diffusion function in (11) does not change the diffusion coefficient dramatically at edges, whereas it turns diffusion less conservative at mottle points.

In our study, we adopt the explicit numerical scheme similar to PM diffusion, given by

$$I^{n+1}(i,j)$$
$$= I^n(i,j) + \Delta t$$
$$\times \left[\begin{array}{c} c_{APNDF,N}^n(i,j)\nabla I_N^n(i,j) + c_{APNDF,S}^n(i,j)\nabla I_S^n(i,j) \\ + c_{APNDF,E}^n(i,j)\nabla I_E^n(i,j) + c_{APNDF,W}^n(i,j)\nabla I_W^n(i,j) \end{array} \right],$$
$$(12)$$

where Δt is the time step with the max $\Delta t = 0.25$ for explicit 2D schemes to achieve stability of the iterative update. Subscripts N, S, E, and W indicate North, South, East, and West, respectively. The directional derivative estimates are defined as follows:

$$\begin{cases} \nabla_N I_{i,j}^n = I_{i-1,j}^n - I_{i,j}^n, & \nabla_S I_{i,j}^n = I_{i+1,j}^n - I_{i,j}^n \\ \nabla_E I_{i,j}^n = I_{i,j+1}^n - I_{i,j}^n, & \nabla_W I_{i,j}^n = I_{i,j-1}^n - I_{i,j}^n. \end{cases} \quad (13)$$

We stop the diffusion by using the mean absolute error (MAE) between two adjacent diffusions.

$$MAE\left(I^{(n)}\right) = \sum_{i=1,j=1}^{i=M,j=N} \left| I^{(n)}(i,j) - I^{(n-1)}(i,j) \right| \Big/ (M \times N),$$
$$(14)$$

where superscript n stands for time sample, $I^{(n-1)}(i,j)$ and $I^{(n)}(i,j)$ are the filtered value at pixel at $(n-1)^{th}$ and $(n)^{th}$ iterations, respectively. M and N are height and width of the processed image. The diffusion process stops automatically when the value of MAE is smaller than a preset threshold ε.

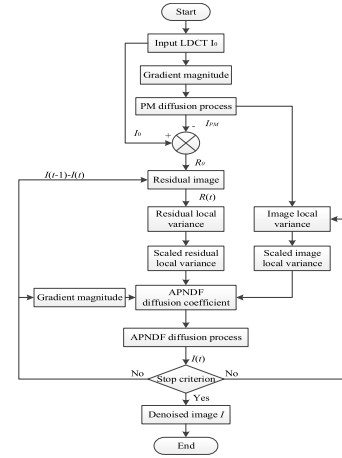The overall ASNDF algorithm is implemented based on the flowchart in Fig. 4.

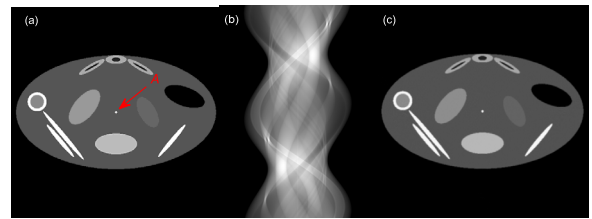**FIGURE 4.** Flowchart of the proposed ASNDF algorithm.

FIGURE 5. Simulated phantom and sinogram data. (a) Simulated phantom image, (b) simulated noise-free sinogram and (c) SDCT image reconstructed from (b).

III. EXPERIMENTAL DESIGN AND RESULTS

In order to evaluate the performance of the proposed ASNDF algorithm, we conducted it on several simulated data, clinical abdomen data and rat data. For comparison study, we compared it with PM model, the IPM model in [40], and the fractional-order differentiation model named FPMTV in [45] which has shown good artifact suppression.

A. DATA SOURCE

1) SIMULATED DATA

The simulation experiment was conducted by using a numerical phantom which is designed based on the ''Shepp-Logan'' phantom and imitates the bones and soft tissues in a real abdominal CT image [18]. The phantom is size of 512×512 and is shown in Fig. 5(a). As to this phantom, a CT model with fan-beam geometry configuration was simulated. The distances of X-ray source to the center of rotation and the detector arrays are 541mm and 949mm, respectively. The detector cell spacing is set to 1 mm. 984 angular samples are acquired on a circular orbit of 360° and the number of bins for each projection view is 731. The simulated sinogram is shown in Fig. 5(b). Fig. 5(c) shows the standard dose CT (SDCT) image reconstructed by FBP from the noise-free projection data in Fig.5 (b). To simulate a LDCT sinogram by a low-dose protocol, we generated a noisy sinogram by adding signal-dependent Gaussian noise to the noise-free projection data, according to the noise model in (15). This noise model was presented by Li *et al.* [10] and Wang *et al.* [52] with

the content that the projection data after system calibration and logarithm transformation was approximately Gaussian distributed, the relation between sample mean and variance being

$$\sigma_{p_s}^2 = f \exp\left(\bar{p}_s / \eta\right), \qquad (15)$$

where $\bar{p}_s$ and $\sigma_{p_s}^2$ is the mean and variance of the projection data at detector bin s. η and f are parameters determined by system settings. For the simulation, the noise level can be controlled by these two parameters.

2) CLINICAL DATA
We used two sets of clinical abdomen data, provided by the Mayo Clinic (USA), to validate the clinical performance of ASNDF processing. The first data is from one person with hemangioma tumor and the second data is from another person with liver cancer. LDCT images with a dose level corresponding to 25% of the full dose were conducted by inserting Poisson noise into the projection data for each case in the library [53]. Each case contains 1mm thickness 512×512 CT images.

3) RAT DATA
The proposed ASNDF processing was also validated using in-vitro rat data with a circular cone-beam geometry. Two acquisitions with different dose were performed on an in-vitro rat. The image size is 892×892 with pixel size of $0.05\text{mm} \times 0.05\text{mm}$.

B. PARAMETER SETTING
The ASNDF method involved three parameters to set, namely: time step Δt in (12), standard variance σ in (11) and stopping threshold ε. We compare our method with other nonlinear diffusion algorithms using the same stopping criterion. We also practically found that the parameter setting could be fixed when processing the LDCT images with the same scan protocol. Parameter settings of different methods for different data are listed in Table 2.

TABLE 2. Parameter setting for different methods.

Method	Phantom	Abdomen	Rat
PM	$\Delta t = 0.2, \sigma = 0.2, \varepsilon = 0.0001$	$\Delta t = 0.01, \sigma = 0.2, \varepsilon = 0.1$	$\Delta t = 0.025, \sigma = 0.2, \varepsilon = 0.1$
IPM	$\Delta t = 0.2, \sigma = 0.2, \varepsilon = 0.0001$	$\Delta t = 0.01, \sigma = 0.2, \varepsilon = 0.1$	$\Delta t = 0.025, \sigma = 0.2, \varepsilon = 0.1$
FPMTV	$\alpha = 1.05, \Delta t = 0.05, \varepsilon = 0.0001$	$\alpha = 1.85, \Delta t = 0.05, \varepsilon = 0.1$	$\alpha = 1.6, \Delta t = 0.05, \varepsilon = 0.1$
ASNDF	$\Delta t = 0.2, \sigma = 0.2, \varepsilon = 0.0001$	$\Delta t = 0.01, \sigma = 0.2, \varepsilon = 0.1$	$\Delta t = 0.025, \sigma = 0.2, \varepsilon = 0.1$

C. PHANTOM DATA STUDY
1) VISUAL ASSESSMENT
In this study, we generated four LDCT projection data by adding signal-dependent Gaussian noise following (15) to the noise-free sinogram as shown in Fig. 5(b). η was fixed to 22,000, and f was respectively set to 100, 200, 300, and 400 to simulate four LDCT projection data with different radiation dose. The corresponding FBP reconstructed LDCT

images with these four dose level are denoted as Recon100, Recon200, Recon300, Recon400, respectively, and are illustrated in the first column (a1, a2, a3, a4) in Fig. 6. We can observe that the LDCT images are severely degraded by the mottle noise and streak artifacts, and a higher f corresponds to a lower radiation and a worse reconstruction with more obvious noise and streak artifacts.

Fig. 6 also depicts the processed results for LDCT images Recon100, Recon200, Recon300 and Recon400 with different methods. From the left to right, the columns correspond to the PM processed images (b1, b2, b3, b4), the IPM processed images (c1, c2, c3, c4), the FPMTV processed images (d1, d2, d3, d4), and our ASNDF processed images (e1, e2, e3, e4). The zoomed regions of interest (ROI) are also illustrated aside. We can observe that the PM method appears effective in removing noise/artifacts and has a good visual effect, yet leading to ''staircase effect'' with a higher f (see zoomed details in b4). We also see that in (c1, c2, c3, c4) that the IPM method only eliminates a part of artifacts, but enhances the residual artifacts to some extent due to its denoising limitation, especially when processing LDCT images with lower radiation dose (see zoomed details in the third column). The FPMTV method can not only reduce noise/artifacts, but also preserve strong structure like object A, however it tends to introduce ambiguity at weak edges (refer to the red arrows in zoomed details in the fourth column). In contrast, the proposed ASNDF method significantly improves the quality of images (e1, e2, e3, e4) without introducing extra artifacts and structure ambiguity. The edges and the small object A are very clear (see the red arrows in the zoomed region in the last column) and the processed result is closest to the phantom image no matter what the dose level of LDCT image is.

Fig. 7 draws the intensity profile along the red dotted line indicated in Fig. 6(a1) for the original phantom image and the processed LDCT images in different cases. We also enlarged the profiles in the same smooth region which is indicated by the black rectangle in Fig. 7. The zoomed profile is displayed in the left-upper corner in each sub-figure. We can observe that all methods have good performances on smoothing and edge preserving when processing Recon100. However, with the decrease of dose, these competing methods obviously do not have good performances on edge preserving and noise removing in the homogenous regions, especially for Recon400. In comparison, the ASNDF method has a much better match to the phantom image for each dose level, it can not only give the best restoration of the homogenous region, but also the edge regions.

2) QUANTITATIVE ASSESSMENT
To evaluate the performance of the proposed method, we calculate two image quality indices with respect to the phantom image: peak signal-to-noise (PSNR) and structural similarity index measurement (SSIM). The PSNR and SSIM represent overall considerations of noise suppression and feature preservation, respectively. The definitions of PSNR, MSE,
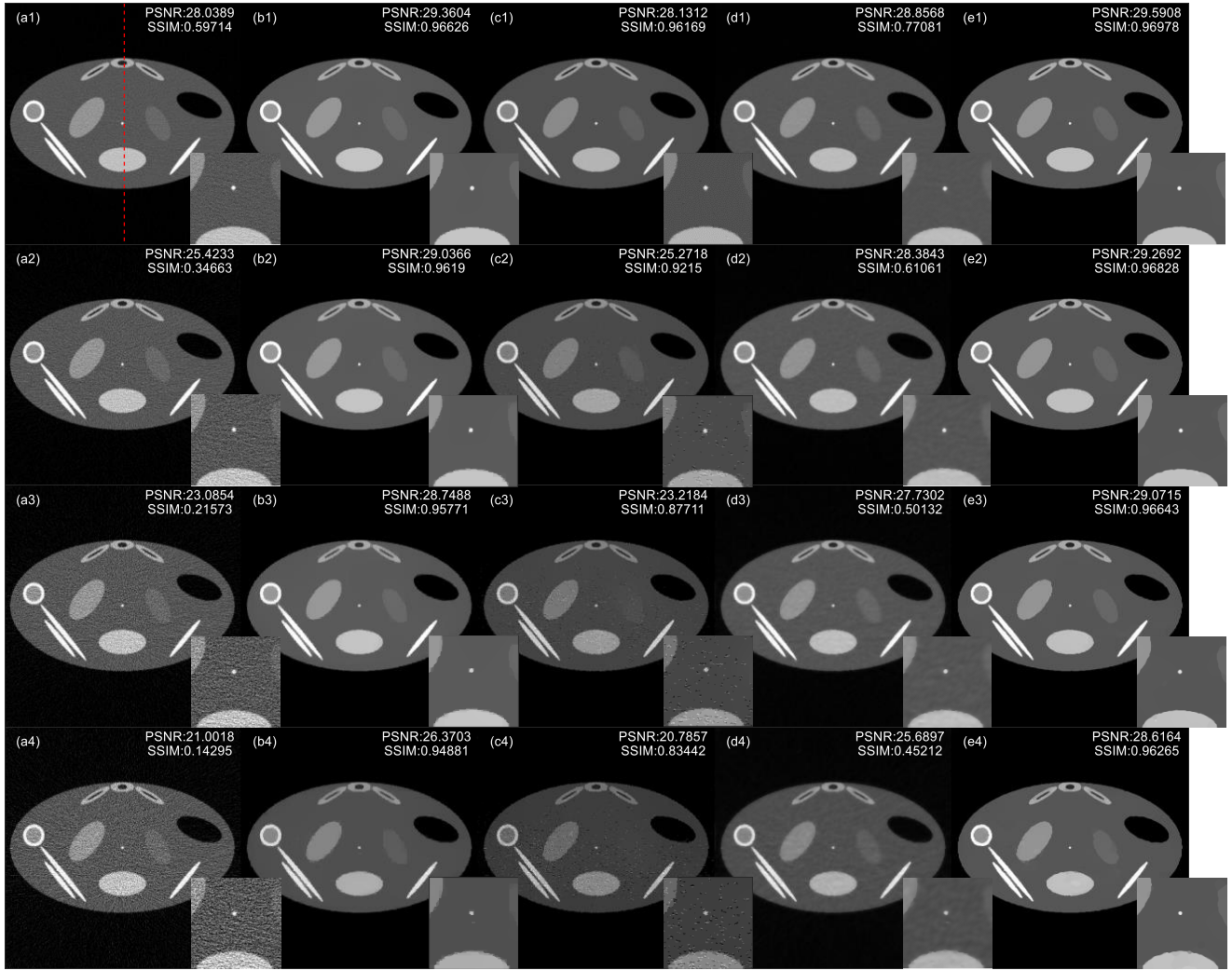
FIGURE 6. Simulated LDCT sinogram data and FBP reconstructed images for the phantom. Images in the first column are the FBP reconstructed images from the simulated LDCT sinogram with different *f*, tagged as Recon100, Recon200, Recon300, and Recon400, respectively. Images in the second column are PM processed LDCT images. Images in the third column are IPM processed LDCT images. Images in the fourth column are FPMTV processed LDCT images. Images in the last column are ASNDF processed LDCT images.

and SSIM are given in (16)-(18).

$$PSNR = 10 \log_{10} \left(\frac{MAX_I^2}{MSE} \right), \quad (16)$$

$$MSE = \frac{1}{MN} \sum_{i=1,j=1}^{i=M,j=N} (I(i,j) - S(i,j))^2, \quad (17)$$

$$SSIM = \frac{(2\mu_S\mu_I + c_1)(2\sigma_{SI} + c_2)}{\left((\mu_S^2 + \mu_I^2 + c_1)(\sigma_S^2 + \sigma_I^2 + c_2)\right)}, \quad (18)$$

where S and μ_S denote the reference phantom and its mean intensity, I and μ_I denotes the processed LDCT image and its mean intensity. σ_S^2 and σ_I^2 are the standard deviations of images S and I. MAX_I is the maximum value of image I. σ_{SI} is the covariance between images S and I. c_1 and c_2 are two constants and more details can be found in [54].

The PSNR and SSIM indices of LDCT images and processed images of different methods are tagged in the right-upper corners in the images in Fig. 6. We can see that the proposed ASNDF method performs better than the competing methods in terms of the two metrics. The PSNR and SSIM values of the processed images are summarized in Table 3. From this table, we can see that the PSNR and SSIM values of the ASNDF processed images are higher than those of other methods, especially the SSIM values are much higher even in the case of lowest radiation dose. This clearly reflects that our proposed method is capable of structure preservation and consistency with the phantom.

3) RESOLUTION ASSESSMENT

Since the modulation transfer function (MTF) is an effective solution to evaluate the resolution preservation, we analyzed the spatial resolution by MTF using the object A in Fig. 5(a) according to [25]. Fig. 8(a)-(d) depicts the MTF curves of the phantom image and the processed LDCT Recon100,
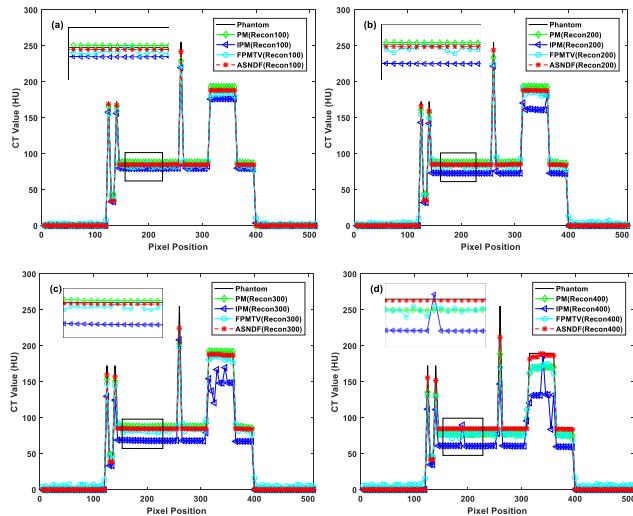
FIGURE 7. Comparison of intensity profiles along the red dotted line indicated in Fig. 6(a1) for the all processed images with different doses. Images (a)-(d) correspond to Recon100, Recon200, Recon300, and Recon400.

TABLE 3. PSNR and SSIM values of the original and processed LDCT images.

		LDCT	PM	IPM	FPMTV	ASNDF
Recon100	PSNR	28.0389	29.3604	28.1312	28.8568	**29.5908**
	SSIM	0.59714	0.96626	0.96169	0.77081	**0.96978**
Recon200	PSNR	25.4233	29.0366	25.2718	28.3843	**29.2692**
	SSIM	0.34663	0.9619	0.9215	0.61061	**0.96828**
Recon300	PSNR	23.0854	28.7488	23.2184	27.7302	**29.0715**
	SSIM	0.21573	0.95771	0.87711	0.50132	**0.96643**
Recon400	PSNR	21.0018	26.3703	20.7857	25.6897	**28.6164**
	SSIM	0.14295	0.94881	0.83442	0.45212	**0.96265**
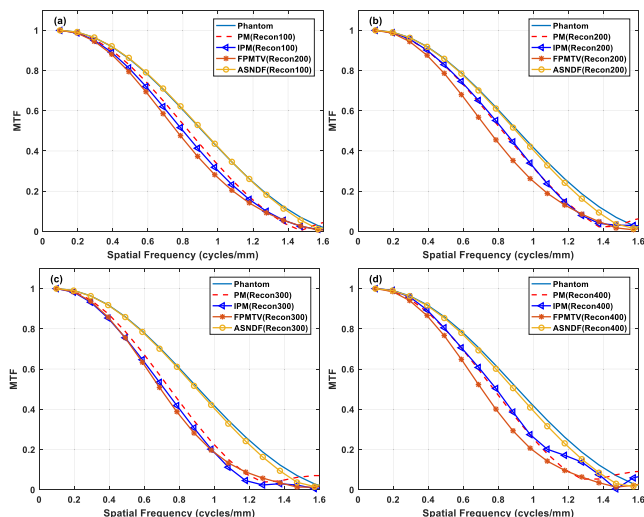
FIGURE 8. Comparison of MTF curves from the original phantom image and the processed images with different dose. Images (a)-(d) correspond to MTF curves of the processed Recon100, Recon200, Recon300, and Recon400.

Recon200, Recon300, and Recon400. We observe that the ASNDF processing leads to the MTF curve most close to that of the phantom image, whereas MTF curves of other methods

are lower than that of the phantom. This demonstrates that the ASNDF processing leads to better spatial resolution than the other methods analyzed the spatial resolution by MTF using the object *A* in Fig. 5(a). Fig. 8(a)-(d) depicts the MTF curves of the phantom image and the processed LDCT Recon100, Recon200, Recon300, and Recon400. We observe that the ASNDF processing leads to the MTF curve most close to that of the phantom image, whereas MTF curves of other methods are lower than that of the phantom. This demonstrates that the ASNDF processing leads to better spatial resolution than the other methods.

D. CLINICAL DATA STUDY
1) VISUAL ASSESSMENT
For Clinical data study, we selected slice #54 and slice #286 for illustration with the display window [80HU, 450HU]. Fig. 9 and Fig. 10 illustrate the processed results for slice #54 and slice #286, respectively. Fig. 9(a1) and Fig. 10(a1) are the original FBP reconstructed LDCT images. Fig. 9(b1) and Fig. 10(b1) are the corresponding reference SDCT images from FBP reconstruction. With the SDCT images as reference, we can observe that serious mottle noise and streak artifacts severely degrade the reconstructed images and lower tissue discrimination. The results of the PM, IPM, FPMTV, and the proposed ASNDF methods are illustrated in the first row (c1, d1, e1, f1) in Figs. 9-10, respectively. Three ROIs containing hemangioma tumor, stomach and spleen tissues, and bones (specified by white squares in Fig. 9(a1)) are enlarged to display in the second, third, and fourth rows, respectively. Also, in Fig. 10, we provide the enlarged ROIs (specified by white squares in Fig. 10(a)) in the second, third, and fourth rows, respectively. The three ROIs contain the information of liver tumor, stomach tissue, and artery vessels. From the images in the third column (c1, c2, c3, c4) in Figs. 9-10, we see that although the PM processing reduce noise/artifacts, but it leads to edge ambiguity (see the yellow arrows in c2, c3, and c4 in Fig. 9 and c4 in Fig. 10). Furthermore, it is not good at preserving small structures, for example, the small structures depicted by yellow ellipse in Fig. 9(a1) are almost disappeared in the PM processed image. As shown in the fourth column in Figs. 9-10, we can see that the IPM processing works well on edge preserving, including small structures (see the red arrow in d3 in Fig. 9), but it cannot remove artifacts effectively. Images in the fifth column in Figs. 9-10 show that FPMTV processed results are visually similar to PM processed results, with better performance on preserving small structures (see the red arrow in e3 in Fig. 9) but worse performance on edge preserving (see the yellow arrows in e2, e3, e4 in Figs. 9-10). In comparison, the proposed ASNDF can effectively reduce noise/artifacts without severe blurring edges. The zoomed ROI images in the last columns in Figs. 9-10 show that our ASNDF method has a better trade-off between structure/edge preserving (see arrows in f2, f3, and f4 in Figs. 9-10) and noise/artifacts reduction.
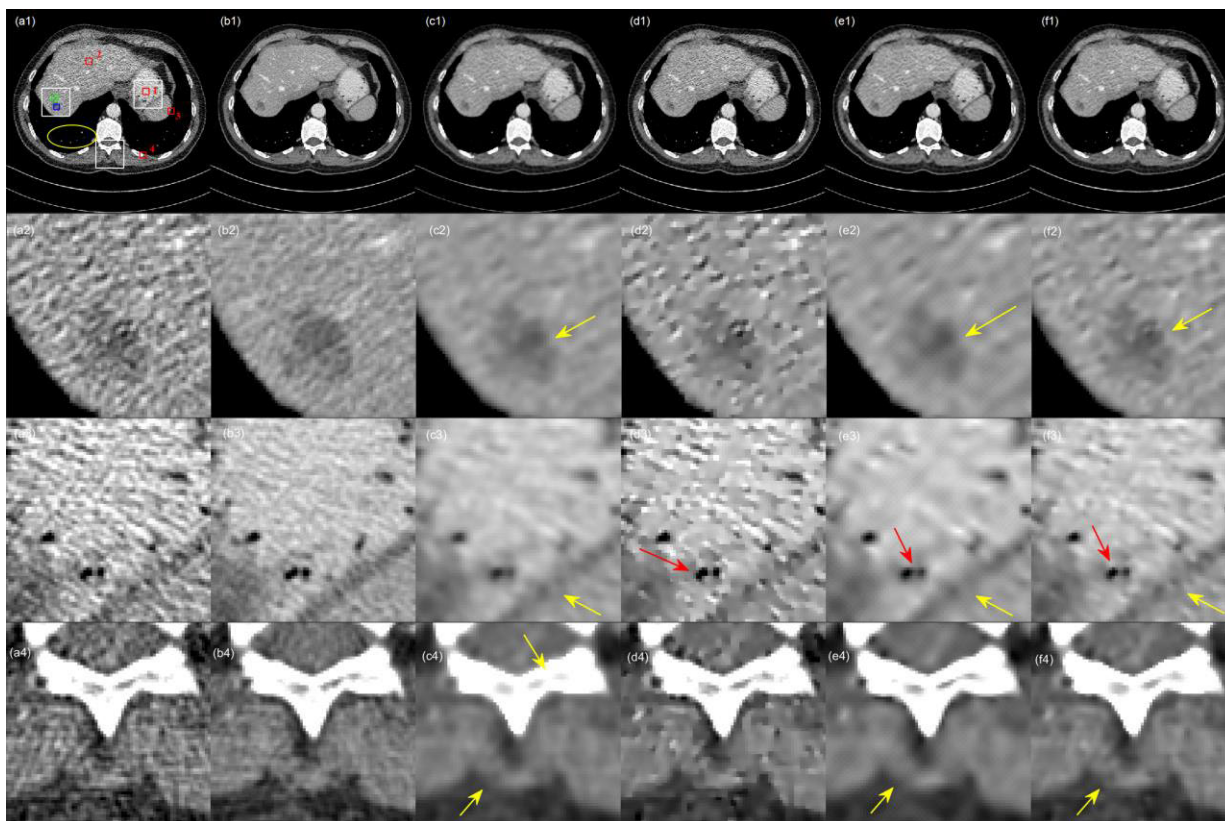
FIGURE 9. The slice #54 of the LDCT data from one patient with hemangioma tumor. From left to right, LDCT image, SDCT image, and the processed images by PM, IPM, FPMTV and ASNDF methods, respectively. From the second row to the bottom, Zoomed ROIs in (a1)-(f1).

2) QUANTITATIVE ASSESSMENT

To evaluate the processed LDCT images, we evaluated the contrast-to-noise ratio (CNR) over the ROI. The CNR measures the contrast between a ROI and the background region. It is generally defined as

$$CNR = |\mu_R - \mu_B| \Big/ \sqrt{\sigma_R^2 + \sigma_B^2}, \qquad (19)$$

where μ_R and σ_R are the mean and standard deviation inside the ROI, μ_B and σ_B are the mean and standard deviation (SD) inside the background region. The SD of ROI and background region is defined as

$$SD_\Omega = \sqrt{\frac{1}{|\Omega| - 1} \sum_{ij \in \Omega} (I_{ij} - \bar{I}_\Omega)^2}, \qquad (20)$$

where I_{ij} and $\bar{I}_\Omega$ denote each point intensity and the mean intensity value inside Ω, respectively.

We calculated the CNR and SD of ROIs for all processed CT images. For slice #54, we calculated the SD of hemangioma tumor region (indicated by the blue square in Fig. 9(a1)) and CNR between the hemangioma tumor region and its surrounding background region (green square region). For slice #286, the liver tumor (indicated by the blue square in Fig. 10(a1)) was chosen as the ROI and the green square region was selected as the background region.

TABLE 4. CNR / SDS of tumor regions in figs. 9-10.

		LDCT	SDCT	PM	IPM	FPMTV	ASNDF
slice	CNR	0.87	1.64	2.3	1.11	2.11	**1.8**
#54	SD	49.81	29.91	20.55	37.87	22.50	**24.6**
slice	CNR	0.45	1.25	1.49	0.49	1.83	**1.32**
#286	SD	58.76	26.12	18.51	55.29	15.47	**20.68**

Table 4 lists the calculated CNR and SD values of the tumor regions in Figs. 9-10. Table 4 indicates that the ASNDF processed images get the closest CNR and SD values to those in SDCT images.

To be specific, we respectively chose anther four regions (specified by red squares) as ROIs from Fig. 9(a1) and Fig. 10(a1) and calculated their SD values. Two homogeneous regions are marked as ROI1 and ROI2, and two edge regions are marked as ROI3 and ROI4. Table 5 lists the calculated SD values for the original LDCT images, the reference SDCT images, and the processed LDCT images. We can clearly see in Table 5 that the ASNDF processed images get closest SD values in homogeneous regions, while the IPM processed images get closest SD values in edge regions, the ASNDF processed images are the second. This shows that the IPM method performs best on edge preserving, however, it cannot remove artifacts effectively. In contrast, the ASNDF method has a good trade-off between noise/artifacts reduction and edge preservation.
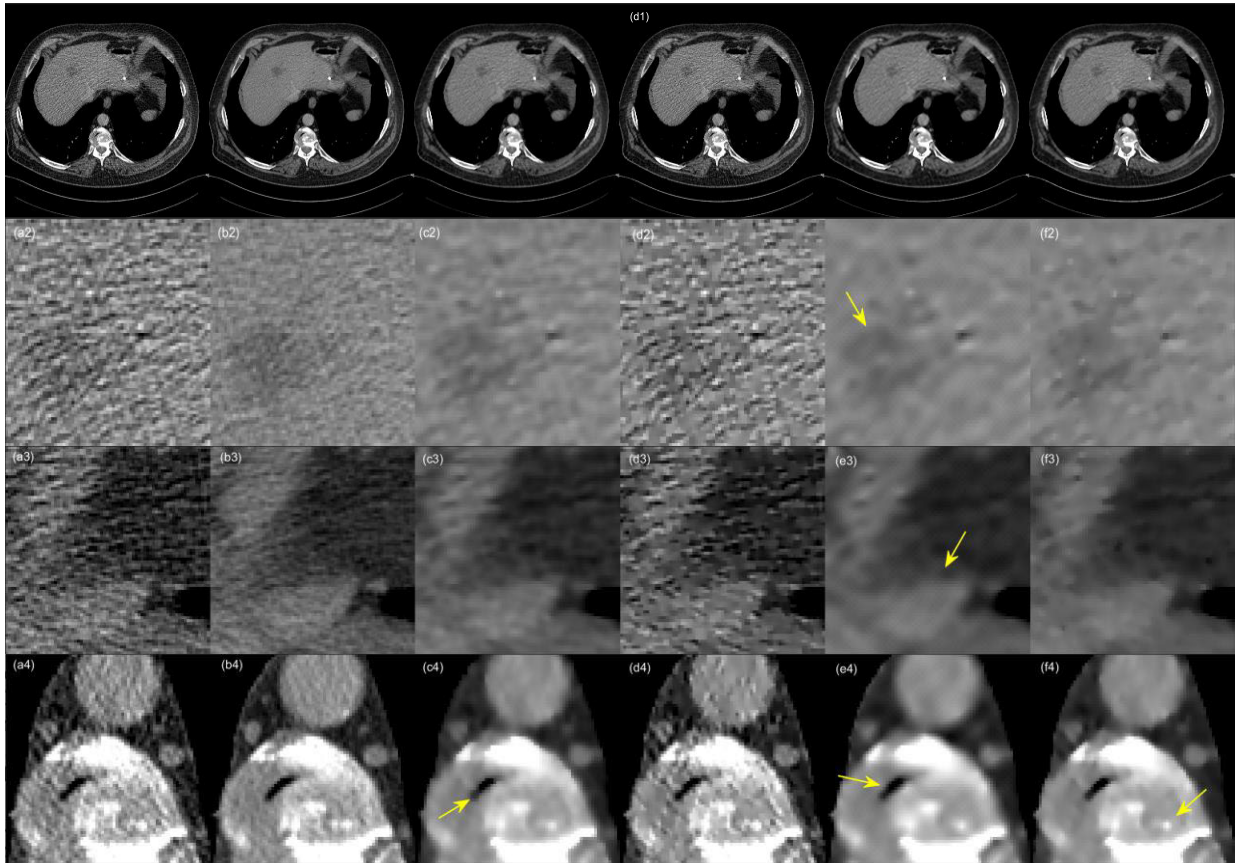
FIGURE 10. The slice #286 of the LDCT data from one patient with liver tumor. From left to right, LDCT image, SDCT image, and the processed images by PM, IPM, FPMTV and ASNDF methods, respectively. From the second row to the bottom, Zoomed ROIs in (a1)-(f1).

TABLE 5. SDS of ROIS (in the red square in figs. 9-10) for the original LDCT images, the original SDCT images and the processed LDCT images.

		LDCT	SDCT	PM	IPM	FPMTV	ASNDF
slice #54	ROI1	60.24	28.65	17.52	47.80	19.23	**24.76**
	ROI2	63.60	28.90	20.29	52.22	23.28	**29.76**
	ROI3	232.81	229.01	225.50	**230.29**	227.01	227.35
	ROI4	478.01	478.17	448.79	**478.61**	465.82	467.49
slice #286	ROI1	58.63	27.66	20.17	54.60	16.74	**22.04**
	ROI2	56.49	21.31	19.49	52.26	17.38	**19.75**
	ROI3	327.06	327.11	318.50	**325.54**	322.92	325.01
	ROI4	371.96	369.91	352.77	**371.36**	356.44	363.02

E. RAT DATA STUDY

1) VISUAL ASSESSMENT

Fig. 11 shows the processed results on the slice #31 of a rat data with display window [250HU, 1300HU]. With the SDCT image in (b1) as reference, we can see that severe noise appears in the original LDCT image in (a1). The processed LDCT images by using PM, IPM, FPMTV, and the proposed ASNDF method are displayed in Fig. 11 (c1)-(d1), respectively. Zoomed images are also given in the second and third rows. We can observe that IPM method suffers from artifacts even it can reduce a lot of noise. The FPMTV processed image in (e1) is not satisfactory both in noise suppression and edge perseving (see the red arrow in (e2)). In contrast, PM method and the proposed FPMTV method

seem to provide images with better trade-off between noise suppression and edge preserving. However, the PM method tends to introduce ''staircase effective'' which is visible in the zoomed image (see the red arrow in (c2)), while we can see a clearer edge in (f2).

2) QUANTITATIVE ASSESSMENT

We calculate SD values upon three tissue ROIs marked by red square in Fig. 11(a1)), and summarize them in Table 6. As illustrated in Table 6, SD values obtained by the proposed ASNDF method are much lower than those obtained by the other methods, which points out that the proposed ASNDF method leads to good noise reduction in homogenous regions. In addition, we can see that most SD values (expect for the one in ROI1) are closer to those of the reference SDCT image.

F. COMPUTATION COST

Compared with the diffusion coefficient function in PM model, twice computation of variance (image local variance and residual local variance) in ASNDF involves an increase in computational complexity. In each iteration, the calculation of image local variance or the residual local image has the biggest time complexity. Both of them have the order of complexity of $O\left(N^2\right)$, where N is the number of pixels in the image. Thus the proposed ASNDF has an order of complexity
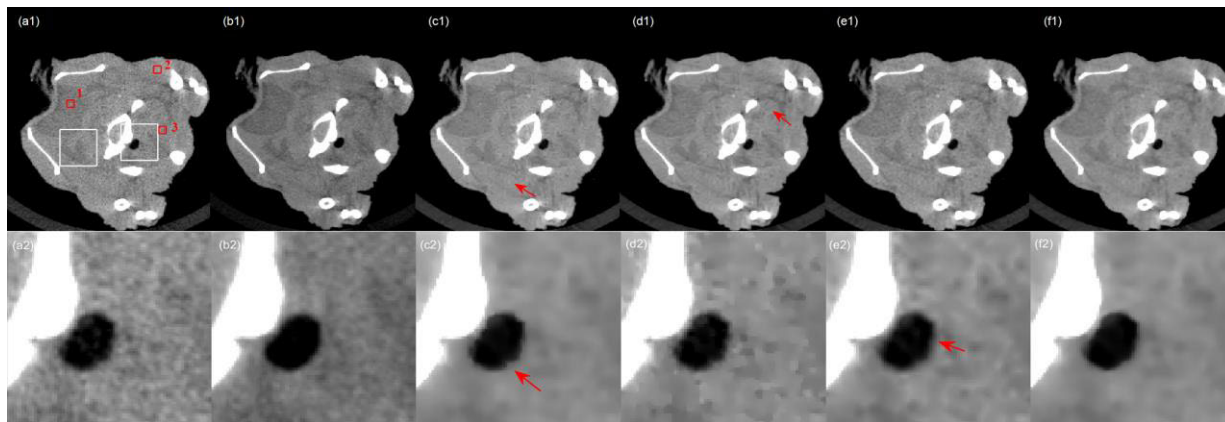
FIGURE 11. Selected axial view for rat data. From left to right, LDCT image, SDCT image, and the processed images by PM, IPM, FPMTV and ASNDF methods, respectively. Zoomed ROIs are displayed in the second row.

TABLE 6. SD values of ROIS (in the red square in fig.11) for the original LDCT images, the original SDCT images and the processed LDCT images.

	LDCT	SDCT	PM	IPM	FPMTV	ASNDF
ROI1	58.33	**32.68**	28.33	44.35	39.93	**27.21**
ROI2	63.14	**33.61**	31.03	42.53	39.93	**31.69**
ROI3	66.93	**39.96**	38.44	49.85	48.63	**38.65**

TABLE 7. Running time (in seconds) of different methods.

	PM	IPM	FPMTV	ASNDF
Simulated LDCT	11.76	7.78	35.48	22.25
Clinical slice	2.12	1.66	3.56	2.53
Rat slice	2.83	2.64	5.85	3.45

of $O\left(K * N^2\right)$, where K is iteration number. The computational complexity of the proposed ASNDF increases as the image size and iteration number increase computational complexity. Fortunately, it can be accelerated after GPU based parallelization.

Table 7 list the running time of different algorithms, all the algorithms are implemented in MATLAB 2016a and accelerated by GPU using parallel computing toolbox. The computer is equipped with CPU i7-8700K @3.70 GHz and 16GB RAM and GPU NVIDIA GeForce GTX 1080Ti. We can observe that ASNDF is faster than FPMTV, but slower than PM and IPM. The reason is that the proposed diffusion function in ASNDF method has three terms, while the diffusion function in PM method or IPM method only has one. In detail, in one iteration, PM method takes about 0.015s, IPM method takes about 0.018s, while the ASNDF method takes about 0.021s.

Although the running time of the ASNDF method is not the least, it doesn't calculate much more time than PM and IPM methods, and is more suitable to be used for clinical data given its good performance on noise/artifacts suppression and edge preserving.

IV. CONCLUSION

This paper described a nonlinear diffusion approach called ASNDF to improve the quality of LDCT images. Instead of only utilizing image gradient magnitude as the cue of edge

indicator, the proposed ASNDF approach also incorporates both image local variance and residual local variance into the design of diffusion coefficient function.

Since the image local variance can distinguish details and noisy background, and the local variance of the residual image can capture lost signals (such as capture weak textures and fine details) in the diffusion procedure, the ASNDF processing is effective in preserving edges, details and small structures. In addition, both the local variance and the residual local variance are not dominant in noise/artifacts, according to which the ASNDF processing encourages diffusion in regions of noise/artifacts. However, the new diffusion factor function simply averages three terms to calculate the diffusion coefficient, and a more appropriate weight allocation in (10) may improve the performance of the algorithm. In any case, the experiments with simulation data, clinical data and rat data, as well as qualitative and quantitative assessments, demonstrate that the proposed ASNDF approach can improve LDCT images. In the future, we will study how the weights affect algorithm performance.

In addition, although we only show two clinical slices and one rat slice, in fact, we tested the proposed ASNDF with the same parameters (as shown in Table 2) on all clinical slices and all rat slices. All processed results are satisfactory. Therefore, the parameter setting of the proposed ASNDF show good robustness in the same scan.

There are also some issues still remain to be addressed. Some streak artifacts are so severe that they could be treated as the structure in the diffusion procedure and may be remained in the final processed LDCT images. So the discrimination of artifacts and image features could be incorporated into the diffusion procedure. Methods like discriminative dictionary in [29] can be considered to discriminate image features and steak artifacts. Additionally, although the proposed method performs well for the streak artifacts caused by noise, it is not very effective for the metal artifacts caused by high-attenuation objects. Finding an effective solution to suppress metal artifacts will be included in our future work.

ACKNOWLEDGMENT

REFERENCES

[1] D. P. Naidich, C. H. Marshall, C. Gribbin, R. S. Arams, and D. I. McCauley, "Low-dose CT of the lungs: Preliminary observations," *Radiology*, vol. 175, no. 3, pp. 729–731, Jun. 1990.

[2] D. J. Brenner, C. D. Elliston, E. J. Hall, and W. E. Berdon, "Estimated risks of radiation-induced fatal cancer from pediatric CT," *AJR Amer. J. Roentgenol.*, vol. 176, no. 2, pp. 289–296, Feb. 2001.

[3] A. E. Stephen, D. L. Segev, D. P. Ryan, M. E. Mullins, S. H. Kim, J. J. Schnitzer, and D. P. Doody, "The diagnosis of acute appendicitis in a pediatric population: To CT or not to CT," *J. Pediatric Surg.*, vol. 38, no. 3, pp. 367–371, Mar. 2003.

[4] M. K. Islam, T. G. Purdie, B. D. Norrlinger, H. Alasti, D. J. Moseley, M. B. Sharpe, J. H. Siewerdsen, and D. A. Jaffray, "Patient dose from kilovoltage cone beam computed tomography imaging in radiation therapy," *Med. Phys.*, vol. 33, no. 6, pp. 1573–1582, Jun. 2006.

[5] G. D. Rubin, "Computed tomography: Revolutionizing the practice of medicine for 40 years," *Radiology*, vol. 273, no. 2S, p. S45–S74, Nov. 2014.

[6] M. K. Kalra, M. M. Maher, T. L. Toth, L. M. Hamberg, M. A. Blake, J.-A. Shepard, and S. Saini, "Strategies for CT radiation dose optimization," *Radiology*, vol. 230, no. 3, pp. 619–628, Mar. 2004. [Online]. Available: http://pubs.rsna.org/doi/10.1148/radiol.2303021726

[7] J. Hsieh, "Adaptive streak artifact reduction in computed tomography resulting from excessive X-ray photon noise," *Med. Phys.*, vol. 25, no. 11, pp. 2139–2147, 1998.

[8] R. D. Lee, "Common image artifacts in cone beam CT," *AADMRT Newslett.*, pp. 1–7, Jul. 2008.

[9] M. Kachelrieß, O. Watzke, and W. A. Kalender, "Generalized multidimensional adaptive filtering for conventional and spiral single-slice, multi-slice, and cone-beam CT," *Med. Phys.*, vol. 28, no. 4, pp. 475–490, 2001.

[10] T. Li, X. Li, J. Wang, J. Wen, H. Lu, J. Hsieh, and Z. Liang, "Nonlinear sinogram smoothing for low-dose X-ray CT," *IEEE Trans. Nucl. Sci.*, vol. 51, no. 5, pp. 2505–2513, Oct. 2004.

[11] J. Wang, T. Li, H. Lu, and Z. Liang, "Penalized weighted least-squares approach to sinogram noise reduction and image reconstruction for low-dose X-ray computed tomography," *IEEE Trans. Med. Imag.*, vol. 25, no. 10, pp. 1272–1283, Oct. 2006.

[12] J. Wang, H. Lu, J. Wen, and Z. Liang, "Multiscale penalized weighted least-squares sinogram restoration for low-dose X-Ray computed tomography," *IEEE Trans. Biomed. Eng.*, vol. 55, no. 3, pp. 1022–1031, Mar. 2008.

[13] A. Manduca, L. Yu, J. D. Trzasko, N. Khaylova, J. M. Kofler, C. M. McCollough, and J. G. Fletcher, "Projection space denoising with bilateral filtering and CT noise modeling for dose reduction in CT," *Med. Phys.*, vol. 36, no. 11, pp. 4911–4919, 2009.

[14] Z. Gui and Y. Liu, "Noise reduction for low-dose X-ray computed tomography with fuzzy filter," *Optik*, vol. 123, pp. 1207–1211, Jul. 2012.

[15] Y. Liu, Q. Zhang, and Z. Gui, "Noise reduction for low-dose CT sinogram based on fuzzy entropy," *J. Electron. Inf. Technol.*, vol. 35, no. 6, pp. 1421–1427, Jun. 2013.

[16] S. W. Lee, Y. Kim, S. S. Shim, J. K. Lee, S. J. Lee, Y. J. Ryu, and J. H. Chang, "Image quality assessment of ultra low-dose chest CT using sinogram-affirmed iterative reconstruction," *Eur. Radiol.*, vol. 24, no. 4, pp. 817–826, Jan. 2014.

[17] S. Zhou, Y. Lu, N. Li, and Y. Wang, "Extension of the virtual electric field model using bilateral-like filter for active contours," *Signal, Image Video Process.*, to be published. doi: 10.1007/s11760-019-01456-x.

[18] Y. Liu, M. Castro, M. Lederlin, A. Kaladji, and P. Haigron, "An improved nonlinear diffusion in Laplacian pyramid domain for cone beam CT denoising during image-guided vascular intervention," *BMC Med. Imag.*, vol. 18, no. 1, p. 25, 2018. doi: 10.1186/s12880-018-0269-1.

[19] J. A. Fessler and A. O. Hero, "Penalized maximum-likelihood image reconstruction using space-alternating generalized EM algorithms," *IEEE Trans. Image Process.*, vol. 4, no. 10, pp. 1417–1429, Oct. 1995.

[20] E. Y. Sidky and X. Pan, "Image reconstruction in circular cone-beam computed tomography by constrained, total-variation minimization," *Phys. Med. Biol.*, vol. 53, no. 17, pp. 4777–4807, 2008.

[21] R. I. Bot and T. Hein, "Iterative regularization with a general penalty term—Theory and application to L1 and TV regularization," *Inverse Problems*, vol. 28, no. 10, pp. 2635–2668, Oct. 2012.

[22] J. H. Jørgensen, E. Sidky, and X. Pan, "Analysis of discrete-to-discrete imaging models for iterative tomographic image reconstruction and compressive sensing," *IEEE Trans. Med. Imag.*, vol. 32, no. 2, pp. 406–474, Feb. 2013.

[23] Y. Chen, J. Ma, Q. Feng, L. Luo, P. Shi, and W. Chen, "Nonlocal prior Bayesian tomographic reconstruction," *J. Math. Imag. Vis.*, vol. 30, no. 2, pp. 133–146, 2008.

[24] B. Li, Q. Lyu, J. Ma, and J. Wang, "Iterative reconstruction for CT perfusion with a prior-image induced hybrid nonlocal means regularization: Phantom studies," *Med. Phys.*, vol. 43, no. 4, pp. 1688–1699, 2016.

[25] J. Wang, T. Li, and L. Xing, "Iterative image reconstruction for CBCT using edge-preserving prior," *Med. Phys.*, vol. 36, no. 1, pp. 252–260, 2009.

[26] H. Zhang, H. Han, J. Wang, J. Ma, Y. Liu, W. Moore, and Z. Liang, "Deriving adaptive MRF coefficients from previous normal-dose CT scan for low-dose image reconstruction via penalized weighted least-squares minimization," *Med. Phys.*, vol. 41, no. 4, 2014, Art. no. 041916.

[27] Y. Liu, M. Castro, M. Lederlin, H. Shu, A. Kaladji, and P. Haigron, "Edge-preserving denoising for intra-operative cone beam CT in endovascular aneurysm repair," *Comput. Med. Imag. Graph.*, vol. 56, pp. 49–59, Mar. 2017.

[28] Z. Li, L. Yu, J. D. Trzasko, D. S. Lake, D. J. Blezek, J. G. Fletcher, C. H. McCollough, and A. Manduca, "Adaptive nonlocal means filtering based on local noise level for CT denoising," *Med. Phys.*, vol. 41, no. 1, 2014, Art. no. 011908.

[29] Y. Chen, X. Bao, X. Yin, L. Luo, and W. Chen, "Improving low-dose X-ray CT images by weighted intensity averaging over large-scale neighborhoods," *Eur. J. Radiol.*, vol. 80, no. 2, pp. e42–e49, Aug. 2011.

[30] Y. Chen, Z. Yang, Y. Hu, G. Yang, Y. Zhu, Y. Li, W. Chen, and C. Toumoulin, "Thoracic low-dose CT image processing using an artifact suppressed large-scale nonlocal means," *Phys. Med. Biol.*, vol. 57, no. 9, pp. 2667–2688, 2012.

[31] Y. Chen, L. Shi, Q. Feng, J. Yang, H. Shu, L. Luo, J.-L. Coatrieux, and W. Chen, "Artifact suppressed dictionary learning for low-dose CT image processing," *IEEE Trans. Med. Imag.*, vol. 33, no. 12, pp. 2271–2292, Dec. 2014.

[32] S. Ghadrdan, J. Alirezaie, J.-L. Dillenseger, and P. Babyn, "Low-dose computed tomography image denoising based on joint wavelet and sparse representation," in *Proc. EMBC*, Aug. 2014, pp. 3325–3328.

[33] D. Kang, P. Slomka, R. Nakazato, J. Woo, D. S. Berman, C.-C. J. Kuo, and D. Dey, "Image denoising of low-radiation dose coronary CT angiography by an adaptive block-matching 3D algorithm," *Proc. SPIE*, vol. 8669, Mar. 2013, Art. no. 86692G.

[34] T. Zhao, J. Hoffman, M. McNitt-Gray, and D. Ruan, "Ultra-low-dose CT image denoising using modified BM3D scheme tailored to data statistics," *Med. Phys.*, vol. 46, no. 1, pp. 190–198, Nov. 2018.

[35] K. Zhang, W. Zuo, Y. Chen, D. Meng, and L. Zhang, "Beyond a Gaussian Denoiser: Residual learning of deep CNN for image denoising," *IEEE Trans. Image Process.*, vol. 26, no. 7, pp. 3142–3155, Jul. 2017.

[36] C. Dong, C. C. Loy, K. He, and X. Tang, "Image super-resolution using deep convolutional networks," *IEEE Trans. Pattern Anal. Mach. Intell.*, vol. 38, no. 2, pp. 295–307, Feb. 2016.

[37] W. Wang, Y. Wang, Y. Wu, T. Lin, S. Li, and B. Chen, "Quantification of full left ventricular metrics via deep regression learning with contour-guidance," *IEEE Access*, vol. 7, pp. 47918–47928, Mar. 2019.

[38] P. Perona and J. Malik, "Scale-space and edge detection using anisotropic diffusion," *IEEE Trans. Pattern Anal. Mach. Intell.*, vol. 12, no. 7, pp. 629–639, Jul. 1990.

[39] Y. Q. Wang, J. Guo, W. Chen, and W. Zhang, "Image denoising using modified Perona–Malik model based on directional Laplacian," *Signal Process.*, vol. 93, no. 9, pp. 2548–2558, Sep. 2013.

[40] S. M. Chao and D. M. Tsai, "An improved anisotropic diffusion model for detail- and edge-preserving smoothing," *Pattern Recognit. Lett.*, vol. 31, no. 13, pp. 2012–2023, Oct. 2010.

[41] Y. Wang, W. Chen, S. Zhou, T. Yu, and Y. Zhang, "MTV: Modified total variation model for image noise removal," *IEEE Trans. Electron. Lett.*, vol. 47, no. 10, pp. 592–594, May 2011.

[42] A. M. Mendrik, E. P. A. Vonken, A. M. R. Schilham, M. A. Viergever, and B. van Ginneken, "Hybrid diffusion compared with existing diffusion schemes on simulated low dose CT scans," presented at the 3rd IEEE Int. Symp. Biomed. Imag., Nano Macro, Arlington, VA, USA, Apr. 2006.

[43] N. Saito, K. Kudo, T. Sasaki, M. Uesugi, K. Koshino, M. Miyamoto, and S. Suzuki, "Realization of reliable cerebral-blood-flow maps from low-dose CT perfusion images by statistical noise reduction using nonlinear diffusion filtering," *Radiol. Phys. Technol.*, vol. 1, pp. 62–74, Jan. 2008.

[44] Z. Yang, S. M. Kaplan, and A. A. Zamyatin, "Multi-resolution diffusion tensor filter for preserving noise power spectrum in low-dose CT imaging," presented at the IEEE Nucl. Sci. Symp. Med. Imag. Conf. Rec. (NSS/MIC), Anaheim, CA, USA, Oct./Nov. 2012.

[45] Y. Wang, Y. Shao, Z. Gui, Q. Zhang, L. Yao, and Y. Liu, "A novel fractional-order differentiation model for low-dose CT image processing," *IEEE Access*, vol. 4, pp. 8487–8499, 2016.

[46] M. W. K. Law and A. C. S. Chung, "Weighted local variance-based edge detection and its application to vascular segmentation in magnetic resonance angiography," *IEEE Trans. Med. Imag.*, vol. 26, no. 9, pp. 1224–1241, Sep. 2007.

[47] X. Liu, S. Chen, M. Zou, and Z. Chai, "Edge-detection based on the local variance in angiographic images," *J. Electron.*, vol. 17, no. 4, pp. 338–344, Oct. 2000.

[48] H. K. Rafsanjani, M. H. Sedaaghi, and S. Saryazdi, "An adaptive diffusion coefficient selection for image denoising," *Digit. Signal Process.*, vol. 64, pp. 71–82, May 2017.

[49] H. Zhong, C. Yang, and X. Zhang, "A new weight for nonlocal means denoising using method noise," *IEEE Signal Process. Lett.*, vol. 19, no. 8, pp. 535–538, Aug. 2012.

[50] Y. Romano and M. Elad, "Improving K-SVD denoising by post-processing its method-noise," in *Proc. ICIP*, Melbourne, VIC, Australia, Sep. 2013, pp. 435–439.

[51] R. Bernardes, C. Maduro, P. Serranho, A. Araújo, S. Barbeiro, and J. Cunha-Vaz, "Improved adaptive complex diffusion despeckling filter," *Opt. Express*, vol. 18, no. 23, pp. 24048–24059, Nov. 2010.

[52] J. Wang, H. Lu, Z. Liang, D. Eremina, G. Zhang, S. Wang, J. Chen, and J. Manzione, "An experimental study on the noise properties of X-ray CT sinogram data in radon space," *Phys. Med. Biol.*, vol. 53, no. 12, pp. 3327–3341, 2008.

[53] *The 2016 NIH-AAPM-Mayo Clinic Low Dose CT Grand Challenge*. Accessed: Jan. 18, 2016. [Online]. Available: http://www.aapm.org/GrandChallenge/LowDoseCT/#

[54] Z. Wang, A. C. Bovik, H. R. Sheikh, and E. P. Simoncelli, "Image quality assessment: From error visibility to structural similarity," *IEEE Trans. Image Process.*, vol. 13, no. 4, pp. 600–612, Apr. 2004.

YANG CHEN is currently with the Laboratory of Image Science and Technology, School of Computer Science and Engineering, Southeast University, Nanjing, China, where he is also with the School of Cyber Science and Engineering and also with the Key Laboratory of Computer Network and Information Integration, Ministry of Education. His research interests include medical image reconstruction, image analysis, pattern recognition, and computerized-aid diagnosis.

PING CHEN received the Ph.D. degree in signal and information processing from the North University of China, in 2014, where he is currently a Professor. His research interests include image processing and image reconstruction.

ZHIWEI QIAO received the Ph.D. degree in transportation information engineering and control from Beijing Jiaotong University, in 2011. He joined the School of Computer and Information Technology, Shanxi University, in 2015. His research interests include medical imaging and signal processing.

YI LIU received the B.S. degree in biomedical engineering and the Ph.D. degree in signal and information processing from the North University of China, in 2009 and 2014, respectively. She was a Postdoctoral Fellow with the Université de Rennes 1, France, from 2014 to 2015. She is currently an Associate Professor with the North University of China. Her research interests include medical imaging and image processing.

ZHIGUO GUI received the Ph.D. degree in signal and information processing from the North University of China, in 2004, where he is currently a Professor. His research interests include image processing and image reconstruction.

• • •